

Multi-Order Matching Network for Alignment-Free Depth Super-Resolution

Zhengxue Wang¹, Zhiqiang Yan^{2*}, Yuan Wu¹, Guangwei Gao¹, Xiang Li³, Jian Yang^{1*}

¹PCA Lab, Nanjing University of Science and Technology

²National University of Singapore ³Nankai University

zwxwang@njust.edu.cn, yanzq@nus.edu.sg

Abstract

Recent guided depth super-resolution methods are premised on the assumption of strictly spatial alignment between depth and RGB, achieving high-quality depth reconstruction. However, in real-world scenarios, the acquisition of strictly aligned RGB-D is hindered by inherent hardware limitations (e.g., physically separate RGB-D sensors) and unavoidable calibration drift induced by mechanical vibrations or temperature variations. Consequently, existing approaches often suffer inevitable performance degradation when applied to misaligned real-world scenes. In this paper, we propose the Multi-Order Matching Network (MOMNet), a novel alignment-free framework that adaptively retrieves and selects the most relevant information from misaligned RGB. Specifically, our method begins with a multi-order matching mechanism, which jointly performs zero-order, first-order, and second-order matching to comprehensively identify RGB information consistent with depth across multi-order feature spaces. To effectively integrate the retrieved RGB and depth, we further introduce a multi-order aggregation composed of multiple structure detectors. This strategy uses multi-order priors as prompts to facilitate the selective feature transfer from RGB to depth. Extensive experiments demonstrate that *MOMNet* achieves state-of-the-art performance and exhibits outstanding robustness.

1. Introduction

Depth super-resolution (DSR) aims to reconstruct high-resolution (HR) depth from degraded low-resolution (LR) counterparts, where HR RGB is often employed as guidance to enhance depth quality. It is widely applied in various downstream tasks, including 3D reconstruction [4, 13, 33, 39], augmented reality [5, 26, 36], and virtual reality [9, 21, 46, 48]. Recently, numerous RGB-guided DSR methods [10, 50, 52, 58] have been proposed. As illustrated in Fig. 1(a), these approaches are typically premised on the

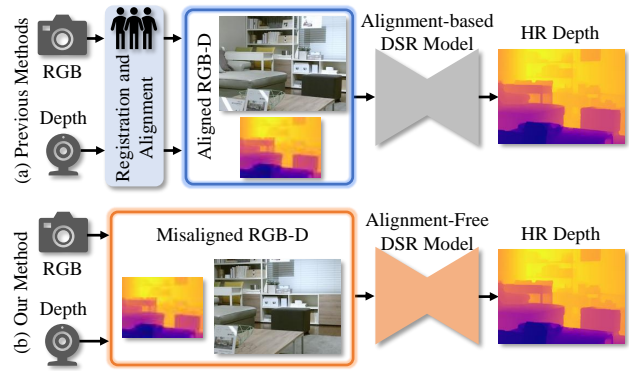


Figure 1. Previous methods (a) are designed based on the assumption of spatial alignment between RGB and depth data. In contrast, our approach (b) focuses more on addressing the misalignment challenges present in real-world scenarios through multi-order matching, enabling alignment-free DSR.

assumption of spatial alignment between RGB and depth, and achieve outstanding performance on aligned RGB-D pairs by developing tailored fusion strategies.

However, in real-world scenarios, obtaining perfectly aligned RGB and depth data is challenging due to hardware limitations and varying imaging conditions. For instance, RGB and depth sensors are typically separate physical modules, making their precise calibration and alignment laborious and costly. Moreover, sensors are often subjected to mechanical vibrations and temperature variations during long-term operation, which can induce calibration drift in registered camera parameters. This makes it difficult for RGB-D sensors to effectively capture strictly spatially aligned data, particularly in consumer-grade devices with inherently limited registration precision. As a result, previous alignment-based DSR methods are highly susceptible to interference from misaligned RGB structure, which severely degrades the accuracy of the recovered HR depth.

To address these issues, we propose an alignment-free multi-order matching framework (MOMNet) that adaptively retrieves and aggregates misaligned RGB features within a multi-order feature space, thereby eliminating the

*Corresponding authors

dependency on spatially aligned data. MOMNet first introduces a multi-order matching to thoroughly mine the depth-relevant RGB information. This mechanism consists of three key components: zero-order matching for original RGB-D features (without derivative calculation), first-order matching for gradient features (first-order derivative), and second-order matching for Hessian features (second-order derivative). Specifically, due to the spatial inconsistency and inherent modality gap between misaligned RGB and depth, relying solely on original zero-order features is insufficient for accurate matching. To this end, we further incorporate first-order and second-order matching to identify structure-related correspondences in the gradient and Hessian domains, respectively. As illustrated in Figs. 2(a) and (b), the resulting gradient and Hessian maps effectively capture structure details. Furthermore, multi-order distribution comparisons reveal a high similarity between RGB and depth, validating the feasibility of matching retrieval in multi-order space. In particular, Figs. 2(c) and (d) show that gradient and Hessian maps provide complementary information in regions (1) and (4), enabling more comprehensive and robust matching. Subsequently, we design a multi-order aggregation strategy that leverages multiple structure detectors to dynamically integrate the retrieved RGB features. Finally, a multi-order regularization is introduced to facilitate the optimization for alignment-free DSR.

Overall, our contributions are as follows:

- We propose a novel DSR solution, termed MOMNet, which leverages multi-order matching, multi-order aggregation, and multi-order regularization to selectively transfer misaligned RGB information to depth.
- To the best of our knowledge, our method is the first alignment-free DSR framework that focuses on addressing the spatial misalignment between RGB and depth in real-world scenes, alleviating the reliance on aligned data.
- Extensive experiments on multiple benchmarks demonstrate the superior robustness and generalization of our method, achieving state-of-the-art performance.

2. Related Work

2.1. Depth Super-Resolution

Recent advances in DSR have been propelled by numerous methods [1, 34, 41, 47, 56], which typically leverage RGB as guidance to reconstruct high-quality HR depth. Existing approaches can be broadly categorized into synthetic [37, 44, 49, 55, 57] and real-world [12, 32, 51] DSR methods. For synthetic DSR, several joint filtering and deep learning methods [16, 22, 43] have been developed to propagate information from RGB to depth. For example, DJFR [23] employs a Convolutional Neural Network (CNN) to perform joint filtering, which selectively fuses consistent salient structure between the guidance and tar-

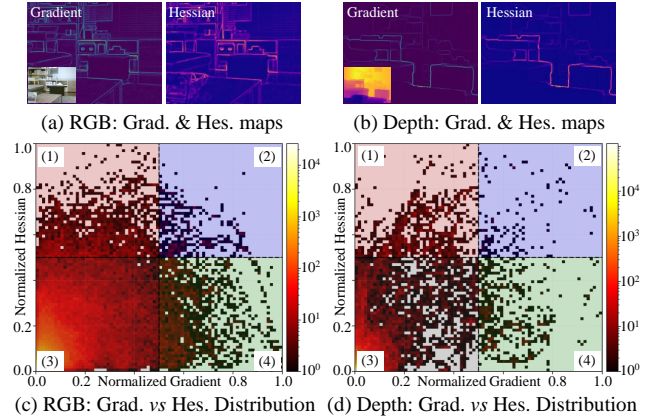


Figure 2. Visualization of Gradient (Grad.) and Hessian (Hes.) maps for (a) RGB and (b) depth, respectively. (c) and (d) present their corresponding distribution comparisons.

get images. DKN [16] integrates a CNN-based architecture to learn sparse and spatially-variant filter kernels, predicting both the relevant neighborhood and corresponding weights for each target pixel. To effectively fuse RGB and depth information, CUNet [6] disentangles cross-modal features into shared and private components via multi-modal convolutional sparse coding. Similarly, DCTNet [54] exploits shared and private convolutional kernels to extract common and modality-specific features respectively. In real-world scenarios, acquired LR depth often suffer from unknown and complex degradation, which poses significant challenges to depth restoration. To address this issue, FDSR [12] introduces a real-world RGB-D dataset and establishes a corresponding baseline for real-world DSR. This approach enhances depth by decomposing and fusing high-frequency components of RGB. More recently, DORNet [45] designs a degradation-oriented framework that learns the implicit degradation representation between LR and HR depth, enabling dynamic depth enhancement. Unlike previous alignment-based methods, we pioneer an alignment-free DSR framework that eliminates the dependency on strictly spatially aligned RGB-D data.

2.2. Feature Matching

Feature matching is a fundamental task in computer vision, aiming to establish point correspondences between images. Recently, a considerable number of feature matching methods [14, 30] have been proposed. For example, LightGlue [25] revisits the sparse matching SuperGlue [30] and proposes a lightweight matching solution. This method predicts a set of correspondences after each computational block, allowing the model to introspect these correspondences and decide whether further computation is necessary. RoMa [7] integrates foundational models by designing a Transformer-based matching decoder, significantly enhancing the robustness of feature match-

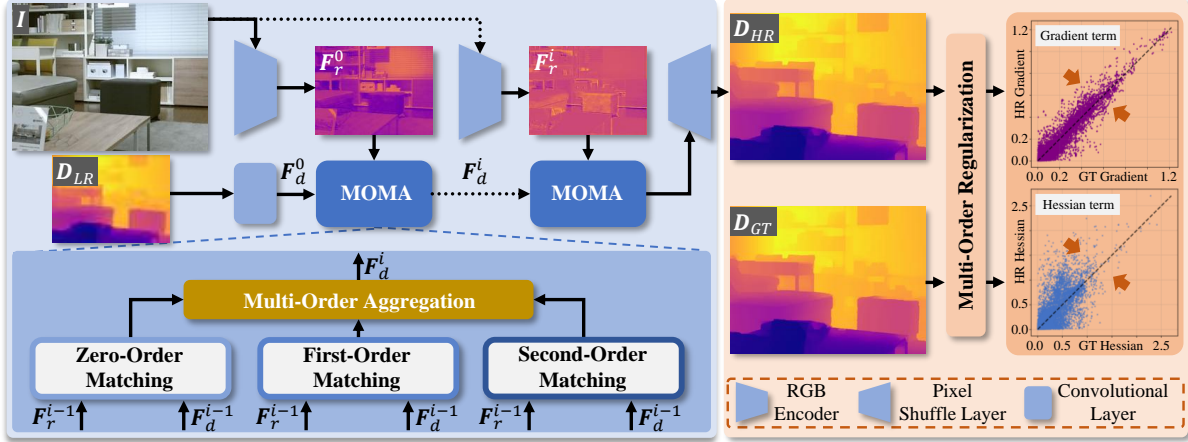


Figure 3. Overview of MOMNet. Given LR depth D_{LR} and RGB I as inputs, we first encode them into features F_d^0 and F_r^0 , respectively. Subsequently, the Multi-Order Matching and Aggregation (MOMA) module is iteratively performed to retrieve and aggregate depth-relevant information from misaligned RGB features, thereby predicting the HR depth D_{HR} . Finally, both D_{HR} and the ground-truth (GT) depth D_{GT} are fed into the Multi-Order Regularization to optimize MOMNet.

ing through regression-by-classification. Similarly, OmniGlue [14] leverages vision foundation models as guidance and introduces a keypoint position-guided attention mechanism to disentangle spatial and appearance information. This approach effectively enhances generalization capability of image matching to unseen real-world scenarios. More recently, MESA [53] employs the image understanding capabilities of segmentation foundation models for a region-level matching approach, constructing a multi-relational graph among regions to enhance accuracy. Different from them, we propose a novel multi-order matching and aggregation strategy that simultaneously performs zero-order, first-order, and second-order matching to retrieve RGB information matching the depth within a multi-order space, effectively enhancing depth features.

2.3. Alignment-Free Learning

Acquiring strictly spatially aligned guidance and target images is often challenging and time-consuming in real-world applications, prompting the development of alignment-free methods [11, 24]. For instance, DCNet [38] introduces an alignment-free RGBT salient object detection network, which leverages spatial affine transformation and feature-level affine transformation to model the correlations between RGB and thermal images. Similarly, SACNet [40] leverages a semantic-guided attention mechanism to learn the relationships between misaligned RGB and thermal images, enabling accurate alignment-free RGBT salient object detection. In addition, IR&ArF [28] designs a spatial-spectral consistent arbitrary-scale observation network to fuse unregistered hyperspectral and multispectral images. In [20], an alignment-free infrared and visible image fusion network is proposed, which utilizes self-attention to achieve the fusion of unregistered images. Unlike previous

approaches, our MOMNet is tailored for RGB-guided DSR, focusing on achieving misaligned and cross-modal fusion between RGB and depth within a multi-order feature space.

3. Method

3.1. Network Architecture

As shown in Fig. 3, given RGB image $I \in R^{sh \times sw \times 3}$ and LR depth $D_{LR} \in R^{h \times w \times 1}$ as inputs, our MOMNet first projects them into feature space using RGB encoder (composed of strided convolutions) and 3×3 convolutional layers, obtaining initial RGB feature F_r^0 and depth feature F_d^0 . s denotes the upsampling factor. h and w are the height and width of LR depth. Then, RGB and depth features are fed into multiple multi-order matching and aggregation (MOMA) modules, which are executed iteratively. These MOMA dynamically retrieve and fuse information corresponding to the depth from the unaligned RGB features, thereby enhancing the depth features. Next, a pixel-shuffle layer is employed to reconstruct the HR depth $D_{HR} \in R^{sh \times sw \times 1}$ from the enhanced depth features. Given the GT depth $D_{GT} \in R^{sh \times sw \times 1}$ and D_{HR} , we further introduce a multi-order regularization that incorporates both first-order gradient and second-order Hessian terms to constrain the learning of MOMNet in a multi-order space.

To better balance computational cost and performance, we introduce a lightweight variant, MOMNet-T. By compressing the intermediate feature channels to $0.25 \times$ of the original and reducing the MOMA iterations to 2, this variant retains only 3.35% parameters of the original MOMNet.

3.2. Multi-Order Matching

As illustrated in the blue part of Fig. 4, our multi-order matching is designed to search for and select the RGB infor-

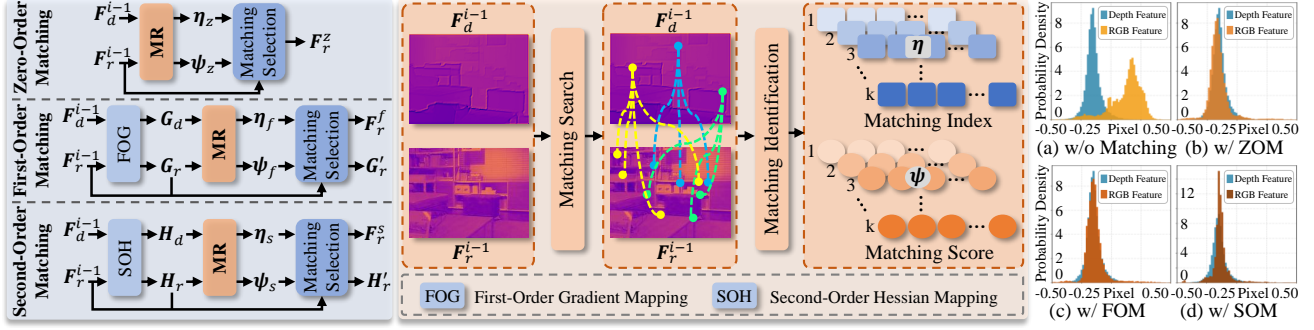


Figure 4. Details of multi-order matching (left) and matching retrieval (MR, middle). Right: histogram comparison of (a) original RGB, (b) zero-order matched (ZOM) RGB, (c) first-order matched (FOM) RGB, and (d) second-order (SOM) matched RGB.

mation most relevant to depth features in multi-order feature space, primarily consisting of zero-order matching, first-order matching, and second-order matching.

Zero-Order Matching. As shown in the first row of Fig. 4 (left), zero-order matching aims to establish the correlation between the original unaligned RGB and depth features. Given the RGB feature F_r^{i-1} and the depth feature F_d^{i-1} as input, we first perform the proposed matching retrieval to compute patch-wise (3×3 patch) correspondence between the RGB and depth features. This process identifies the k most relevant RGB patches for each depth patch, yielding matching index η_z and matching score ψ_z .

Then, based on the predicted matching indices and scores, we introduce a matching selection strategy that adaptively selects RGB patches matching the depth features from the input RGB features. These patches are aggregated to obtain the zero-order matched RGB features F_r^z :

$$F_r^z = f_r \left(\sum_{j=1}^k f_p(\eta_z^j, F_r^{i-1}) \otimes \tau(\psi_z^j) \right), \quad (1)$$

where f_p denotes the index-based RGB patch extraction operation. f_r refers to a reshape operation that transforms patches into the same dimensions as the RGB feature F_r^{i-1} . $\tau(\cdot)$ is softmax function. \otimes is element-wise multiplication.

First-Order Matching. To mitigate the interference caused by the inherent cross-modal discrepancies in RGB-D data during matching retrieval, we introduce first-order matching for robust retrieval. As depicted in the second row of Fig. 4 (left), we first calculate the first-order derivatives of the original RGB feature F_r^{i-1} and depth feature F_d^{i-1} , obtaining the RGB gradient representation G_r and depth gradient representation G_d . Taking the RGB as an example, the gradient mapping process is formulated as:

$$G_r = \sqrt{\left(\frac{\partial F_r^{i-1}}{\partial x} \right)^2 + \left(\frac{\partial F_r^{i-1}}{\partial y} \right)^2}. \quad (2)$$

Subsequently, we perform a matching retrieval between the RGB gradient G_r and the depth gradient G_d in the

gradient space, obtaining matching index η_f and matching score ψ_f . A selection strategy analogous to Eq.(1) is then applied to extract components from the original RGB features that correspond to the depth gradient, yielding the first-order matched RGB feature F_r^f .

Furthermore, we leverage η_f and ψ_f to filter the original RGB gradient G_r , producing the first-order matching matched G_r^f :

$$G_r^f = f_r \left(\sum_{j=1}^k f_p(\eta_f^j, G_r) \otimes \tau(\psi_f^j) \right). \quad (3)$$

Second-Order Matching. Compared to first-order gradient, the second-order Hessian representation can reveal more intricate local geometric structure. As shown in the third row of Fig. 4 (left), we further introduce second-order matching for thorough retrieval of high-frequency information. Specifically, given the original RGB feature F_r^{i-1} , we first compute its Hessian matrix and the corresponding Frobenius norm to obtain RGB Hessian representation H_r :

$$H_r = \sqrt{\left(\frac{\partial^2 F_r^{i-1}}{\partial x^2} \right)^2 + \left(\frac{\partial^2 F_r^{i-1}}{\partial y^2} \right)^2 + 2 \left(\frac{\partial^2 F_r^{i-1}}{\partial x \partial y} \right)^2}. \quad (4)$$

Similarly, we apply the same operation as in Eq. (4) to the original depth feature F_d^{i-1} , thereby resulting in depth Hessian representation H_d . Then, we conduct matching retrieval to predict the second-order matching index η_s and matching score ψ_s between RGB and depth Hessian representations. Finally, F_r^{i-1} , H_d , η_s , and ψ_s are fed together into the matching selection module (analogous to Eqs. (1) and (3)) to dynamically generate the second-order matched RGB feature F_r^s and RGB Hessian representation H_r^s .

Matching Retrieval. As depicted in Fig. 4 (middle), given RGB and depth features as input, matching retrieval first performs a matching search by computing the correlation between target depth patch and all RGB patches, resulting in a correlation set $\mathbb{C} \in R^{hw \times hw}$. Taking zero-order matching as an example, the correlation set \mathbb{C}_z is defined as:

$$\mathbb{C}_z = \phi(\rho(F_d^{i-1}), \rho(F_r^{i-1})), \quad (5)$$

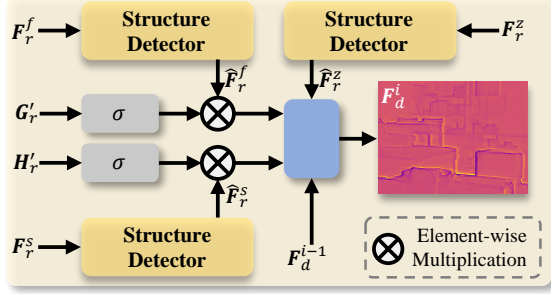


Figure 5. Details of multi-order aggregation. σ : Sigmoid Layer.

where $\rho(\cdot)$ and $\phi(\cdot)$ are the 3×3 patch extraction operation and the cosine similarity function, respectively.

We then retrieve the most relevant RGB information by identifying the top- k patches from the correlation set \mathbb{C}_z to enhance the depth representation:

$$\eta_z, \psi_z = \text{top}K(\mathbb{C}_z), \quad (6)$$

where $\eta_z \in R^{hw \times k}$ and $\psi_z \in R^{hw \times k}$ are matching indices and scores of top- k matched RGB patches, respectively.

Fig. 4 (right) compares the feature distributions of multi-order matched RGB features against depth features. As shown in (a), a significant distribution discrepancy arises from the spatial misalignment between RGB and depth. In contrast, (b)-(d) reveal that zero-order, first-order, and second-order matching strategies effectively retrieve RGB features that are more consistent with the depth representation, thereby substantially reducing the distribution gap.

3.3. Multi-Order Aggregation

Based on the retrieved zero-order, first-order, and second-order RGB features, the multi-order aggregation is designed to selectively transfer RGB information to the depth. As shown in Fig. 5, the multi-order aggregation mainly consists of multiple structure detectors and convolutional layers. Each detector takes F_r^z , F_r^f , and F_r^s as inputs to extract depth-relevant structure features while suppressing texture noise present in the RGB, generating \hat{F}_r^z , \hat{F}_r^f , and \hat{F}_r^s .

Next, we utilize the gradient G_r^f and Hessian H_r^f as prompts to dynamically aggregate the detected RGB structure with the depth feature F_d^{i-1} :

$$F_d^i = f_c(\cup(F_d^{i-1}, \hat{F}_r^z, \sigma(G_r^f) \otimes \hat{F}_r^f, \sigma(H_r^f) \otimes \hat{F}_r^s)), \quad (7)$$

where F_d^i represents the fused depth features, while f_c , \cup , and $\sigma(\cdot)$ denote the convolutional layer, the concatenation operation, and the sigmoid function, respectively.

Structure Detector. The cross-modal discrepancy between RGB and depth often causes undesirable interference from RGB textures during the fusion process, which hinders depth enhancement. To this end, we introduce a novel learnable structure detector based on the Hessian matrix.

Algorithm 1 Structure Detector

Require: Input RGB feature $F_r \in \mathbb{R}^{c \times h \times w}$

- 1: **Step 1: Initialize Input**
- 2: $F_{norm} \leftarrow \text{Normalize}(F_r)$
- 3: $F_{comp} \leftarrow \text{Channel Compression}(F_{norm})$
- 4: **Step 2: Hessian Computation**
- 5: Hessian: $\mathcal{H}(F_{comp}(x, y)) = \begin{bmatrix} \frac{\partial^2 F_{comp}}{\partial x^2} & \frac{\partial^2 F_{comp}}{\partial x \partial y} \\ \frac{\partial^2 F_{comp}}{\partial y \partial x} & \frac{\partial^2 F_{comp}}{\partial y^2} \end{bmatrix}$
- 6: $\lambda_1, \lambda_2 \leftarrow \text{Eigenvalue Calculation}(\mathcal{H}(F_{comp}(x, y)))$
- 7: Sort eigenvalues: $|\lambda_1| \geq |\lambda_2|$
- 8: **Step 3: Structure Detection**
- 9: Initialize the learnable parameters α and β .
- 10: Structure Awareness: $E \leftarrow \left(1 - \exp\left(-\frac{|\lambda_1|}{\alpha + \epsilon}\right)\right)$
- 11: Texture Suppress: $T_{suppress} \leftarrow \exp\left(-\frac{|\lambda_1 \otimes \lambda_2|}{\beta + \epsilon}\right)$
- 12: Geometric Mask: $M_{geom} \leftarrow \mathbb{I}[\lambda_2 < 0]$
- 13: Structure Descriptor: $S \leftarrow E \otimes T_{suppress} \otimes M_{geom}$
- 14: **Step 4: Structure Extraction**
- 15: $\hat{F}_r = \text{RefineNet}(S) \otimes F_r$
- 16: **return** Structure-enhanced RGB feature \hat{F}_r

Drawing on the principles of the Frangi filter [8], the absolute values and sign of Hessian eigenvalues reflect the surface curvature and structure type, respectively. Specifically, texture-rich corner regions typically exhibit high curvature in both directions, resulting in two large eigenvalues. For edge or structure regions, the curvature is high along the normal direction but low along tangent, yielding an eigenvalue pair with a pronounced magnitude disparity. Conversely, flat regions are characterized by two small eigenvalues, with curvature in both directions approaching zero.

Based on the above analysis, our detector adaptively identifies geometric structure in RGB features by utilizing second-order derivative characteristics, while suppressing texture noise. As outlined in Alg. 1, the structure detector first employs eigenvalue decomposition to establish a triple-constraint mechanism comprising structure awareness, texture suppression, and geometric mask. Taking RGB features (e.g., F_r^z , F_r^f , and F_r^s) as input, the detector predicts a structure descriptor S :

$$S = \underbrace{\left(1 - \exp\left(-\frac{|\lambda_1|}{\alpha + \epsilon}\right)\right)}_{\text{structure awareness}} \otimes \underbrace{\exp\left(-\frac{|\lambda_1 \otimes \lambda_2|}{\beta + \epsilon}\right)}_{\text{texture suppression}} \otimes \underbrace{\mathbb{I}[\lambda_2 < 0]}_{\text{geometric mask}}, \quad (8)$$

where ϵ is set to 1×10^{-8} , and $\mathbb{I}[\cdot]$ is the indicator function. $\exp(\cdot)$ denotes the exponential function. Then, S is used to filter input features through a lightweight refinement net-

Table 1. Quantitative comparison (RMSE in centimeters) between our MOMNet and previous state-of-the-art approaches.

Methods	Hypersim			DIML			DyDToF			Average			Venue
	×4	×8	×16	×4	×8	×16	×4	×8	×16	×4	×8	×16	
DJF [22]	17.35	25.59	38.01	2.20	3.94	7.31	5.60	8.40	12.78	8.38	12.64	19.37	ECCV 2016
DJFR [23]	15.93	23.43	36.71	2.09	3.43	7.01	4.89	7.60	12.30	7.64	11.49	18.67	PAMI 2019
CUNet [6]	15.59	21.95	32.72	2.08	3.21	5.66	4.66	7.05	11.11	7.44	10.74	16.50	PAMI 2020
FDKN [16]	12.74	20.11	31.47	2.18	3.24	5.61	3.44	6.29	10.70	6.12	9.88	15.93	IJCV 2021
DKN [16]	12.42	19.98	31.25	2.13	3.32	5.67	3.43	6.25	10.57	5.99	9.85	15.83	IJCV 2021
FDSR [12]	11.63	19.06	28.89	2.01	2.93	4.99	3.21	6.04	9.85	5.62	9.34	14.58	CVPR 2021
DCTNet [54]	12.69	21.85	32.06	1.98	3.20	5.48	3.44	6.66	10.69	6.04	10.57	16.08	CVPR 2022
SUFT [31]	9.35	16.04	26.60	1.85	3.03	4.89	2.75	4.84	8.74	4.65	7.97	13.41	MM 2022
DADA [27]	15.82	23.39	33.37	2.24	3.48	5.99	5.08	7.95	12.28	7.71	11.61	17.21	CVPR 2023
SGNet [42]	<u>8.27</u>	15.72	25.74	1.79	2.86	4.76	<u>2.68</u>	4.77	8.54	<u>4.25</u>	7.78	13.01	AAAI 2024
DORNet [45]	10.10	18.82	28.89	1.93	3.19	5.33	2.80	5.85	9.93	4.94	9.29	14.72	CVPR 2025
C2PD [15]	9.71	<u>15.06</u>	<u>24.11</u>	1.93	2.87	<u>4.71</u>	2.91	<u>4.74</u>	<u>8.44</u>	4.85	<u>7.56</u>	<u>12.42</u>	AAAI 2025
MOMNet-T	11.32	17.80	26.88	1.66	2.76	<u>4.71</u>	3.37	5.47	8.93	5.45	8.68	13.51	-
MOMNet	7.57	14.14	23.37	<u>1.67</u>	<u>2.81</u>	4.47	2.41	4.41	7.89	3.88	7.12	11.91	-

work (comprising three convolutional layers and a sigmoid layer), yielding the structure-enhanced RGB features.

3.4. Multi-Order Regularization

Given the GT depth D_{GT} and the predicted HR depth D_{HR} , we introduce a multi-order regularization to optimize our MOMNet in a multi-order space. Specifically, we first incorporate a common reconstruction loss \mathcal{L}_{rec} to facilitate high-quality depth reconstruction:

$$\mathcal{L}_{rec} = \sum_{n \in \mathbb{N}} \|D_{GT}^n - D_{HR}^n\|_1, \quad (9)$$

where $\|\cdot\|_1$ denotes the L_1 norm, while \mathbb{N} represents the set of valid pixels in the GT depth.

Then, we further employ first-order gradient \mathcal{L}_{grad} and second-order Hessian \mathcal{L}_{hes} terms to promote the learning of high-frequency components.

$$\begin{aligned} \mathcal{L}_{grad} &= \sum_{n \in \mathbb{N}} \|\Phi(D_{GT}^n) - \Phi(D_{HR}^n)\|_1, \\ \mathcal{L}_{hes} &= \sum_{n \in \mathbb{N}} \|\Upsilon(D_{GT}^n) - \Upsilon(D_{HR}^n)\|_1, \end{aligned} \quad (10)$$

where Φ and Υ represent the gradient mapping and the Hessian mapping, as defined in Eqs. (2) and (4), respectively.

The total loss function \mathcal{L}_{total} is defined as:

$$\mathcal{L}_{total} = \mathcal{L}_{rec} + \mathcal{L}_{grad} + \alpha \mathcal{L}_{hes}, \quad (11)$$

where α refers to hyper-parameters.

4. Experiments

4.1. Experimental Setups

Datasets. To evaluate MOMNet, we utilize three public datasets with consecutive frames to synthesize spatially unaligned data, including Hypersim [29], DIML [2, 3, 17–19], and DyDToF [35] datasets. Specifically, we first randomly select 1500 pairs of unaligned RGB and depth data from the

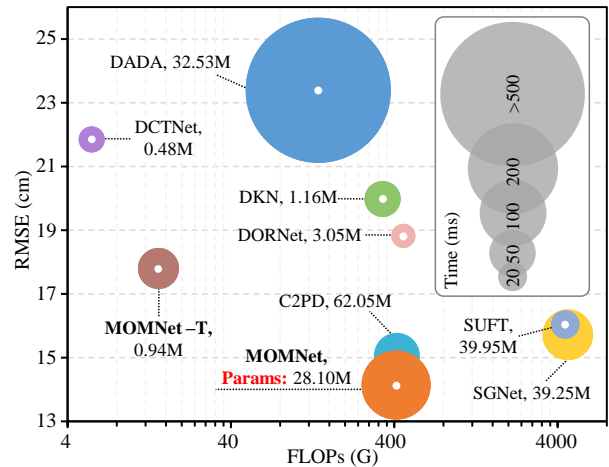


Figure 6. Complexity comparison on ×8 Hypersim tested by a 4090 GPU. Larger circle area indicates longer inference time.

fully simulated Hypersim dataset for the training set, and 100 pairs for the test set. Then, the pre-trained weights from the Hypersim dataset are directly applied to test DIML (100 RGB-D pairs) and DyDToF (100 RGB-D pairs) datasets without any fine-tuning, thereby evaluating the generalization capability. Following previous methods [16, 54], all LR depth are generated from GT depth using bicubic downsampling. Additionally, to ensure a fair comparison, we retrain and evaluate our MOMNet and all comparison approaches under the same datasets and settings.

Implementation Details. Consistent with existing methods [12, 42], we select root mean square error (RMSE) in centimeters as the evaluation metric. The Adam optimizer with an initial learning rate of 1×10^{-4} is used to train our method. Besides, we implement MOMNet on a single NVIDIA 4090 GPU. The hyperparameter α is set to 0.001.

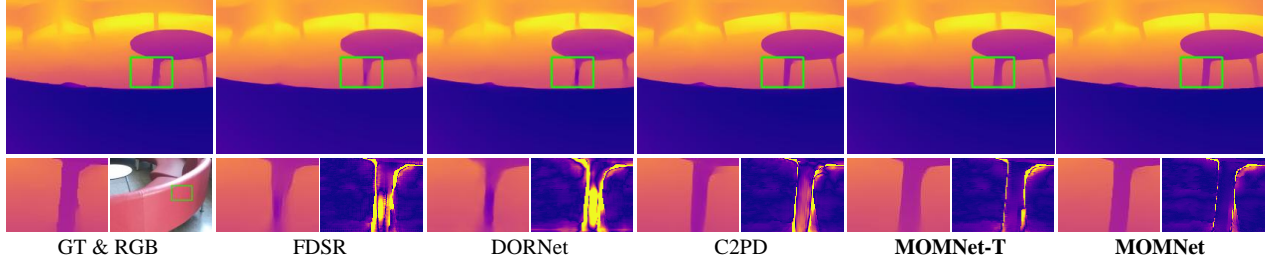


Figure 7. Visual results (left) and error maps (right) on the DIML dataset ($\times 16$). Brighter color in error maps denotes larger error.

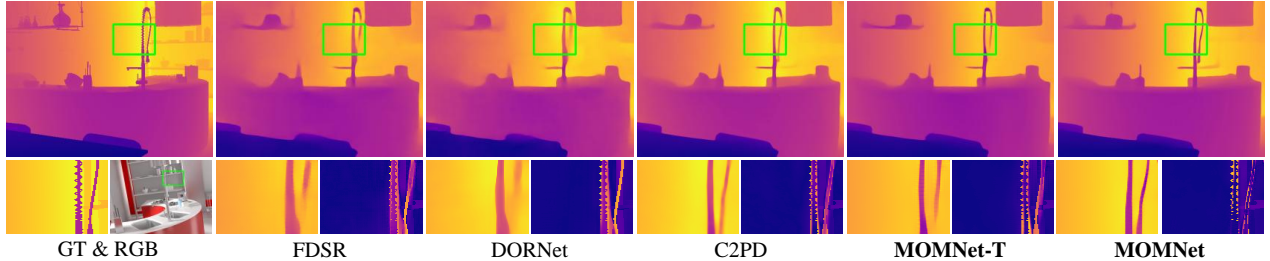


Figure 8. Visual results (left) and error maps (right) for noise robustness (standard deviation 0.07) on the Hypersim dataset.

4.2. Comparison with the State-of-the-Art

Quantitative Comparison. As shown in Tab. 1, MOMNet demonstrates satisfactory performance across all datasets and scale factors. For example, our method outperforms the suboptimal approach by $0.70cm$ ($\times 4$) and $0.92cm$ ($\times 8$) in RMSE on the Hypersim, respectively. For large-scale factor DSR, MOMNet also achieves the lowest RMSE ($\times 16$), surpassing the second-best C2PD [15] by an average of $0.51cm$ across the three datasets. Moreover, our lightweight MOMNet-T also delivers highly competitive performance, with an average RMSE advantage of $2.57cm$ over DCT-Net [54] and $1.21cm$ over DORNet [45] in $\times 16$ DSR.

Visual Comparison. Fig. 7 presents a visual comparison with state-of-the-art methods on the DIML dataset, demonstrating that our approach effectively reconstructs high-quality depth from misaligned RGB and LR depth inputs. It is evident that the depth of the table legs predicted by our MOMNet is closer to the ground truth, with fewer errors. Please see our appendix for more visual results.

Model Complexity analysis. As shown in Fig. 6, our method achieves a competitive balance between performance and model complexity. Compared to the suboptimal C2PD [15], our MOMNet exhibits comparable computational cost while achieving a significant performance improvement, reducing the parameter count by $33.95M$ and further lowering the RMSE by $0.92cm$. For lightweight DSR, MOMNet-T also delivers satisfactory performance. It surpasses the latest DORNet [45] by achieving an additional performance improvement of $1.02cm$, while reducing the number of parameters by $2.11M$ and FLOPs by $440.22G$.

Robustness to Noise. To further validate the robustness of MOMNet, Fig. 9 presents a quantitative compari-

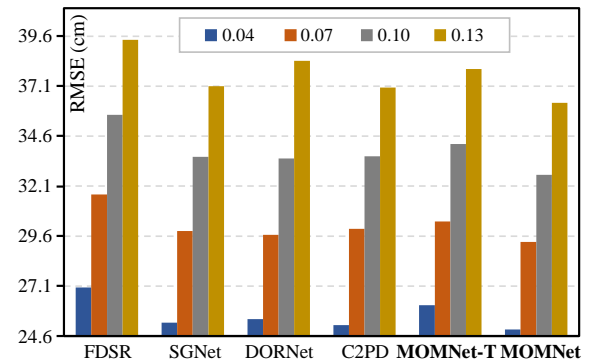


Figure 9. Robustness to different gaussian noise (standard deviation ranging from 0.04 to 0.13) on the $\times 8$ Hypersim dataset.

son across different noise levels. Similar to previous approaches [16, 45], we add Gaussian noise (mean 0, standard deviation ranging from 0.04 to 0.13) to the LR depth as new input. These results indicate that our method achieves excellent noise robustness, consistently attaining the lowest RMSE under all noise levels. For example, MOMNet achieves RMSE improvements of $0.35cm$ and $0.83cm$ over the suboptimal method at standard deviations of 0.07 and 0.10, respectively. Furthermore, Fig. 9 provides a visual comparison of joint denoising and DSR. It can be observed that our method effectively recovers clear depth structure in noisy environments. For instance, the reconstructed water pipe is more discriminative than others.

4.3. Ablation Studies

Multi-Order Matching. Tab. 2 presents the ablation study of zero-order, first-order, and second-order matching. For the baseline (a), we remove all matching modules and use

Table 2. Ablation study of zero-order matching (ZOM), first-order matching (FOM), and second-order matching (SOM) on $\times 8$ DSR.

Methods	ZOM	FOM	SOM	Hypersim	DyDToF
(a)				15.31	4.66
(b)	✓			14.51	4.62
(c)		✓		14.83	4.52
(d)			✓	14.67	4.57
(e)	✓	✓		14.28	4.48
(f)	✓		✓	14.39	4.51
(g)		✓	✓	14.51	4.51
(h)	✓	✓	✓	14.14	4.41

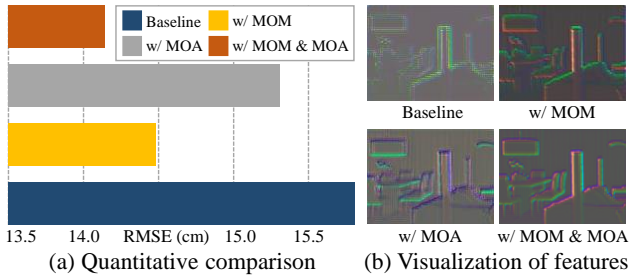


Figure 10. Ablation study of multi-order matching (MOM) and multi-order aggregation (MOA) on $\times 8$ Hypersim.

the original RGB input to replace all matched RGB features. Compared with (a), (b)–(d) demonstrate that each individual matching algorithm consistently improves performance. Furthermore, (e)–(g) validate the complementarity of multi-order matching, showing that it is more effective to enhance reconstruction quality than any single matching. When all three are combined, our method (h) achieves the best performance, reducing RMSE by $1.17cm$ on Hypersim and $0.25cm$ on DyDToF compared with the baseline. In summary, these results fully confirm the effectiveness and synergistic benefits of our multi-order matching strategy.

MOMA. Fig. 10(a) depicts the ablation study of multi-order matching (MOM) and multi-order aggregation (MOA). For the baseline, we remove all MOM and MOA from MOMNet and use addition to fuse the misaligned RGB-D. The results clearly show that both MOM and MOA contribute performance gains over the baseline. When combined, our method achieves the best results, surpassing the baseline by $1.67cm$ RMSE on the Hypersim dataset. Additionally, Fig. 10(b) visualizes the depth features using principal component analysis (PCA), showing that both MOM and MOA effectively enhance the depth structure.

Furthermore, Fig. 11(a) illustrates the results with different numbers of multi-order matching and aggregation (MOMA). It can be seen that the error progressively decreases as the number of iterations increases. When the number exceeds 3, the declining trend of the RMSE gradually plateaus. To balance model complexity and performance, we adopt 3 iterations as the default setting.

Table 3. Ablation study of different loss functions on $\times 8$ DSR.

Methods	Hypersim	DyDToF
Baseline	14.25	4.47
Baseline + \mathcal{L}_{grad}	14.16	4.44
Baseline + \mathcal{L}_{hes}	14.22	4.46
Baseline + $\mathcal{L}_{grad} + \mathcal{L}_{hes}$	14.14	4.41

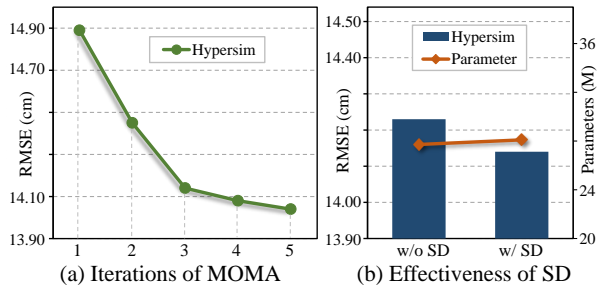


Figure 11. Ablation study of MOMNet with (a) MOMA numbers and (b) effectiveness of structure detector (SD) on $\times 8$ Hypersim.

Different Loss Functions. Tab. 3 lists the ablation study of different loss functions. The baseline model removes both the first-order gradient term \mathcal{L}_{grad} and the second-order Hessian term \mathcal{L}_{hes} from the multi-order regularization, retaining only the zero-order reconstruction term \mathcal{L}_{rec} . Compared to the baseline, incorporating either \mathcal{L}_{grad} or \mathcal{L}_{hes} individually leads to performance gains. When all three terms are combined, our MOMNet achieves the best performance, surpassing the baseline by $0.11cm$ in RMSE on the Hypersim dataset and $0.06cm$ in RMSE on the DyDToF dataset.

Structure Detector. Fig. 11(b) reports the ablation study of the structure detector (SD). These results demonstrate that SD effectively contributes to performance improvement with only a minor increase in parameters. For instance, SD successfully reduces the RMSE by $0.09cm$ on the Hypersim dataset while introducing only $0.38M$ additional parameters. Please refer to our appendix for more experiments.

5. Conclusion

In this paper, we propose MOMNet, a novel framework that pioneers an alignment-free paradigm for RGB-guided DSR. To alleviate the reliance on strictly spatially aligned RGB-D data, our method first collaboratively identifies RGB content relevant to depth by performing multi-order matching across zero-order, first-order, and second-order feature space. Based on multi-order priors, we further design a multi-order aggregation strategy that dynamically transfers the matched RGB information to depth representation using the structure detector. Additionally, a multi-order regularization is introduced to facilitate the optimization of our MOMNet, thereby enhancing geometric consistency in the predicted depth. Extensive experiments demonstrate the superiority and robustness of our MOMNet.

References

- [1] Xuanhong Chen, Hang Wang, Jialiang Chen, Kairui Feng, Jinfan Liu, Xiaohang Wang, Weimin Zhang, and Bingbing Ni. Intrinsic phase-preserving networks for depth super-resolution. In *AAAI*, pages 1210–1218, 2024. 2
- [2] Jaehoon Cho, Dongbo Min, Youngjung Kim, and Kwanghoon Sohn. Deep monocular depth estimation leveraging a large-scale outdoor stereo dataset. *Expert Systems with Applications*, 178:114877, 2021. 6
- [3] Jaehoon Cho, Dongbo Min, Youngjung Kim, and Kwanghoon Sohn. Diml/cvl rgb-d dataset: 2m rgb-d images of natural indoor and outdoor scenes. *arXiv preprint arXiv:2110.11590*, 2021. 6
- [4] Jaesung Choe, Sunghoon Im, Francois Rameau, Minjun Kang, and In So Kweon. Volumefusion: Deep depth fusion for 3d scene reconstruction. In *ICCV*, pages 16086–16095, 2021. 1
- [5] Riccardo De Lutio, Alexander Becker, Stefano D’Aronco, Stefania Russo, Jan D Wegner, and Konrad Schindler. Learning graph regularisation for guided super-resolution. In *CVPR*, pages 1979–1988, 2022. 1
- [6] Xin Deng and Pier Luigi Dragotti. Deep convolutional neural network for multi-modal image restoration and fusion. *IEEE Transactions on Pattern Analysis and Machine Intelligence*, 43(10):3333–3348, 2020. 2, 6
- [7] Johan Edstedt, Qiyu Sun, Georg Bökman, Mårten Wadenbäck, and Michael Felsberg. Roma: Robust dense feature matching. In *CVPR*, pages 19790–19800, 2024. 2
- [8] Alejandro F Frangi, Wiro J Niessen, Koen L Vincken, and Max A Viergever. Multiscale vessel enhancement filtering. In *MICCAI*, pages 130–137. Springer, 1998. 5
- [9] Xiao Gu, Yao Guo, Fani Deligianni, and Guang-Zhong Yang. Coupled real-synthetic domain adaptation for real-world deep depth enhancement. *IEEE Transactions on Image Processing*, 29:6343–6356, 2020. 1
- [10] Chunle Guo, Chongyi Li, Jichang Guo, Runmin Cong, Huazhu Fu, and Ping Han. Hierarchical features driven residual learning for depth map super-resolution. *IEEE Transactions on Image Processing*, 28(5):2545–2557, 2018. 1
- [11] Chengmei Han, Lei Liu, Kunpeng Wang, Fei Xie, and Bing Wei. Hierarchical semantics guided multi-scale correlation network for alignment-free red-green-blue and thermal salient object detection. *Engineering Applications of Artificial Intelligence*, 162:112394, 2025. 3
- [12] Lingzhi He, Hongguang Zhu, Feng Li, Huihui Bai, Runmin Cong, Chunjie Zhang, Chunyu Lin, Meiqin Liu, and Yao Zhao. Towards fast and accurate real-world depth super-resolution: Benchmark dataset and baseline. In *CVPR*, pages 9229–9238, 2021. 2, 6
- [13] Tak-Wai Hui, Chen Change Loy, and Xiaoou Tang. Depth map super-resolution by deep multi-scale guidance. In *ECCV*, pages 353–369, 2016. 1
- [14] Hanwen Jiang, Arjun Karapur, Bingyi Cao, Qixing Huang, and André Araujo. Omnigluue: Generalizable feature matching with foundation model guidance. In *CVPR*, pages 19865–19875, 2024. 2, 3
- [15] Jiahui Kang, Qing Cai, Runqing Tan, Yimei Liu, and Zhi Liu. C2pd: Continuity-constrained pixelwise deformation for guided depth super-resolution. In *AAAI*, pages 4212–4220, 2025. 6, 7
- [16] Beomjun Kim, Jean Ponce, and Bumsuh Ham. Deformable kernel networks for joint image filtering. *International Journal of Computer Vision*, 129(2):579–600, 2021. 2, 6, 7
- [17] Sunok Kim, Dongbo Min, Bumsuh Ham, Seungryong Kim, and Kwanghoon Sohn. Deep stereo confidence prediction for depth estimation. In *ICIP*, pages 992–996, 2017. 6
- [18] Youngjung Kim, Bumsuh Ham, Changjae Oh, and Kwanghoon Sohn. Structure selective depth superresolution for rgb-d cameras. *IEEE Transactions on Image Processing*, 25(11):5227–5238, 2016.
- [19] Youngjung Kim, Hyungjoo Jung, Dongbo Min, and Kwanghoon Sohn. Deep monocular depth estimation via integration of global and local predictions. *IEEE Transactions on Image Processing*, 27(8):4131–4144, 2018. 6
- [20] Huafeng Li, Junyu Liu, Yafei Zhang, and Yu Liu. A deep learning framework for infrared and visible image fusion without strict registration. *International Journal of Computer Vision*, 132(5):1625–1644, 2024. 3
- [21] Ling Li, Xiaojuan Li, Shanlin Yang, Shuai Ding, Alireza Jolfaei, and Xi Zheng. Unsupervised-learning-based continuous depth and motion estimation with monocular endoscopy for virtual reality minimally invasive surgery. *IEEE Transactions on Industrial Informatics*, 17(6):3920–3928, 2020. 1
- [22] Yijun Li, Jia-Bin Huang, Narendra Ahuja, and Ming-Hsuan Yang. Deep joint image filtering. In *ECCV*, pages 154–169, 2016. 2, 6
- [23] Yijun Li, Jia-Bin Huang, Narendra Ahuja, and Ming-Hsuan Yang. Joint image filtering with deep convolutional networks. *IEEE Transactions on Pattern Analysis and Machine Intelligence*, 41(8):1909–1923, 2019. 2, 6
- [24] Zan Li, Yue Wen, Song Xiao, Jiahui Qu, Nan Li, and Wenqian Dong. A progressive registration-fusion co-optimization a-mamba network: Towards deep unregistered hyperspectral and multispectral fusion. *IEEE Transactions on Geoscience and Remote Sensing*, 2025. 3
- [25] Philipp Lindenberger, Paul-Edouard Sarlin, and Marc Pollefeys. Lightglue: Local feature matching at light speed. In *ICCV*, pages 17627–17638, 2023. 2
- [26] Xianming Liu, Deming Zhai, Rong Chen, Xiangyang Ji, Debin Zhao, and Wen Gao. Depth restoration from rgb-d data via joint adaptive regularization and thresholding on manifolds. *IEEE Transactions on Image Processing*, 28(3):1068–1079, 2018. 1
- [27] Nando Metzger, Rodrigo Caye Daudt, and Konrad Schindler. Guided depth super-resolution by deep anisotropic diffusion. In *CVPR*, pages 18237–18246, 2023. 6
- [28] Jiahui Qu, Xiaoyang Wu, Wenqian Dong, Jizhou Cui, and Yunsong Li. Ir&arf: Towards deep interpretable arbitrary resolution fusion of unregistered hyperspectral and multispectral images. *IEEE Transactions on Image Processing*, 2025. 3
- [29] Mike Roberts, Jason Ramapuram, Anurag Ranjan, Atulit Kumar, Miguel Angel Bautista, Nathan Paczan, Russ Webb,

- and Joshua M Susskind. Hypersim: A photorealistic synthetic dataset for holistic indoor scene understanding. In *ICCV*, pages 10912–10922, 2021. 6
- [30] Paul-Edouard Sarlin, Daniel DeTone, Tomasz Malisiewicz, and Andrew Rabinovich. Superglue: Learning feature matching with graph neural networks. In *CVPR*, pages 4938–4947, 2020. 2
- [31] Wuxuan Shi, Mang Ye, and Bo Du. Symmetric uncertainty-aware feature transmission for depth super-resolution. In *ACMMM*, pages 3867–3876, 2022. 6
- [32] Xibin Song, Yuchao Dai, Dingfu Zhou, Liu Liu, Wei Li, Hongdong Li, and Ruigang Yang. Channel attention based iterative residual learning for depth map super-resolution. In *CVPR*, pages 5631–5640, 2020. 2
- [33] Hang Su, Varun Jampani, Deqing Sun, Orazio Gallo, Erik Learned-Miller, and Jan Kautz. Pixel-adaptive convolutional neural networks. In *CVPR*, pages 11166–11175, 2019. 1
- [34] Baoli Sun, Xinchun Ye, Baopu Li, Haojie Li, Zhihui Wang, and Rui Xu. Learning scene structure guidance via cross-task knowledge transfer for single depth super-resolution. In *CVPR*, pages 7792–7801, 2021. 2
- [35] Zhanghao Sun, Wei Ye, Jinhui Xiong, Gyeongmin Choe, Jialiang Wang, Shuo Chen Su, and Rakesh Ranjan. Consistent direct time-of-flight video depth super-resolution. In *CVPR*, pages 5075–5085, 2023. 6
- [36] Jiayang Tang, Xiaokang Chen, and Gang Zeng. Joint implicit image function for guided depth super-resolution. In *ACMMM*, pages 4390–4399, 2021. 1
- [37] Qi Tang, Runmin Cong, Ronghui Sheng, Lingzhi He, Dan Zhang, Yao Zhao, and Sam Kwong. Bridgenet: A joint learning network of depth map super-resolution and monocular depth estimation. In *ACMMM*, pages 2148–2157, 2021. 2
- [38] Zhengzheng Tu, Zhun Li, Chenglong Li, and Jin Tang. Weakly alignment-free rgb salient object detection with deep correlation network. *IEEE Transactions on Image Processing*, 31:3752–3764, 2022. 3
- [39] Jun Wang, Peilin Liu, and Fei Wen. Self-supervised learning for rgb-guided depth enhancement by exploiting the dependency between rgb and depth. *IEEE Transactions on Image Processing*, 32:159–174, 2022. 1
- [40] Kunpeng Wang, Danying Lin, Chenglong Li, Zhengzheng Tu, and Bin Luo. Alignment-free rgb salient object detection: Semantics-guided asymmetric correlation network and a unified benchmark. *IEEE Transactions on Multimedia*, 26:10692–10707, 2024. 3
- [41] Xiaohang Wang, Xuanhong Chen, Bingbing Ni, Zhengyan Tong, and Hang Wang. Learning continuous depth representation via geometric spatial aggregator. In *AAAI*, pages 2698–2706, 2023. 2
- [42] Zhengxue Wang, Zhiqiang Yan, and Jian Yang. Sgnet: Structure guided network via gradient-frequency awareness for depth map super-resolution. In *AAAI*, pages 5823–5831, 2024. 6
- [43] Zhengxue Wang, Zhiqiang Yan, Ming-Hsuan Yang, Jinshan Pan, Jian Yang, Ying Tai, and Guangwei Gao. Scene prior filtering for depth map super-resolution. *arXiv preprint arXiv:2402.13876*, 2024. 2
- [44] Zhengxue Wang, Yuan Wu, Xiang Li, Zhiqiang Yan, and Jian Yang. Spatiotemporal difference network for video depth super-resolution. *arXiv preprint arXiv:2508.01259*, 2025. 2
- [45] Zhengxue Wang, Zhiqiang Yan, Jinshan Pan, Guangwei Gao, Kai Zhang, and Jian Yang. Dornet: A degradation oriented and regularized network for blind depth super-resolution. In *CVPR*, pages 15813–15822, 2025. 2, 6, 7
- [46] Zhiqiang Yan, Kun Wang, Xiang Li, Guangwei Gao, Jun Li, and Jian Yang. Tri-perspective view decomposition for geometry aware depth completion and super-resolution. *IEEE Transactions on Pattern Analysis and Machine Intelligence*, 2025. 1
- [47] Yuxiang Yang, Qi Cao, Jing Zhang, and Dacheng Tao. Codon: On orchestrating cross-domain attentions for depth super-resolution. *International Journal of Computer Vision*, 130(2):267–284, 2022. 2
- [48] Xinchun Ye, Baoli Sun, Zhihui Wang, Jingyu Yang, Rui Xu, Haojie Li, and Baopu Li. Depth super-resolution via deep controllable slicing network. In *ACMMM*, pages 1809–1818, 2020. 1
- [49] Xinchun Ye, Baoli Sun, Zhihui Wang, Jingyu Yang, Rui Xu, Haojie Li, and Baopu Li. Pmbanet: Progressive multi-branch aggregation network for scene depth super-resolution. *IEEE Transactions on Image Processing*, 29:7427–7442, 2020. 2
- [50] Xinchun Ye, Aokai Zhang, and Rui Xu. Semantics-driven contrastive learning for real-world depth super resolution. In *ACMMM*, pages 3085–3093, 2025. 1
- [51] Jiayi Yuan, Haobo Jiang, Xiang Li, Jianjun Qian, Jun Li, and Jian Yang. Structure flow-guided network for real depth super-resolution. In *AAAI*, pages 3340–3348, 2023. 2
- [52] Jialong Zhang, Lijun Zhao, Jinjing Zhang, Anhong Wang, and Huihui Bai. Joint deep-unfolding optimization learning for depth map arbitrary-scale super-resolution. *IEEE Transactions on Multimedia*, 2025. 1
- [53] Yesheng Zhang and Xu Zhao. Mesa: Matching everything by segmenting anything. In *CVPR*, pages 20217–20226, 2024. 3
- [54] Zixiang Zhao, Jianshe Zhang, Shuang Xu, Zudi Lin, and Hanspeter Pfister. Discrete cosine transform network for guided depth map super-resolution. In *CVPR*, pages 5697–5707, 2022. 2, 6, 7
- [55] Zixiang Zhao, Jianshe Zhang, Xiang Gu, Chengli Tan, Shuang Xu, Yulun Zhang, Radu Timofte, and Luc Van Gool. Spherical space feature decomposition for guided depth map super-resolution. In *ICCV*, pages 12547–12558, 2023. 2
- [56] Huan Zheng, Wen Cheng Han, and Jianbing Shen. Decoupling fine detail and global geometry for compressed depth map super-resolution. In *CVPR*, pages 951–960, 2025. 2
- [57] Zhiwei Zhong, Xianming Liu, Junjun Jiang, Debin Zhao, Zhiwen Chen, and Xiangyang Ji. High-resolution depth maps imaging via attention-based hierarchical multi-modal fusion. *IEEE Transactions on Image Processing*, 31:648–663, 2021. 2
- [58] Man Zhou, Keyu Yan, Jinshan Pan, Wenqi Ren, Qi Xie, and Xiangyong Cao. Memory-augmented deep unfolding network for guided image super-resolution. *International Journal of Computer Vision*, 131(1):215–242, 2023. 1